Structure and ferromagnetic instability of the oxygen-deficient SrTiO$_3$ surface

Soham S. Ghosh[1] and Efstratios Manousakis[1,2,*]

[1]*Department of Physics and National High Magnetic Field Laboratory, Florida State University, Tallahassee, Florida 32306-4350, USA*
[2]*Department of Physics, University of Athens, Panepistimioupolis, Zografos, 157 84 Athens, Greece*

SrTiO$_3$ (STO) is the substrate of choice to grow oxide thin films and oxide heterojunctions, which can form quasi-two-dimensional electronic phases that exhibit a wealth of phenomena, and thus a workhorse in the emerging field of metal-oxide electronics. Hence, it is of great importance to know the exact character of the STO surface itself under various oxygen environments. Using density functional theory within the spin generalized gradient approximation we have investigated the structural, electronic, and magnetic properties of the oxygen-deficient STO surface. We find that the surface oxygen vacancies order in periodic arrays giving rise to surface magnetic moments and a quasi-two-dimensional electron gas in the occupied Ti 3d orbitals. The surface confinement, the oxygen-vacancy ordering, and the octahedra distortions give rise to spin-polarized t_{2g} dispersive subbands; their energy split near the Brillouin zone center acts as an effective Zeeman term, which, when we turn on a Rashba interaction, produces bands with momentum-spin correlations similar to those recently discovered on oxygen-deficient STO surface.

I. INTRODUCTION

The interface between two transition-metal oxides forms quasi-two-dimensional electronic phases [1–4] that exhibit a rich set of phenomena, including tunable insulator-superconductor-metal transitions [5,6], large magnetoresistance [7], ferromagnetism [7], and superconductivity [8–10]. The perovskite SrTiO$_3$ (STO) is the substrate used for many such heterojunctions, and therefore it plays a crucial role in the area of metal-oxide interfaces [11,12]. Although it is a nonmagnetic wideband insulator in bulk with a band gap of 3.2 eV [1], a quasi-two-dimensional electron gas (Q2DEG) with interesting spin-momentum correlations has been detected on its surface [13–17]. This Q2DEG can be produced through multiple methods, such as gating [6,18], by creating surface oxygen vacancies [13,14] or by inserting a δ-doped layer [19–22] inside the bulk crystal.

As seen by angle-resolved photoemission spectroscopy (ARPES), the Q2DEG has a strongly confined component made up of two subbands, separated from each other by about 90 meV, forming concentric circular sections of the Fermi surface (FS) [13,17], and a relatively less strongly confined component, about 200 meV higher in energy, forming ellipsoidal sections of the FS [14]. *Ab initio* [23,24] and model [25,26] calculations have identified Ti t_{2g} as the host states, although there are open questions about the nature of the Q2DEG. The two concentric rings of the FS on the k_x-k_y plane are made up of $3d_{xy}$ orbitals, and two ellipsoids aligned along the k_x and k_y directions are $3d_{xz}/d_{yz}$ states in nature [14]. The $3d_{xz}/d_{yz}$ states are quasi-one-dimensional, and as seen from layer-by-layer ARPES study [27] on LaTiO$_3$/SrTiO$_3$ interface, they have bulklike behavior. These FS features have been seen to be created by intense ultraviolet irradiation [17]. They persist under varying levels of oxygen vacancies and annealing conditions [14], and thus seem ubiquitous.

At titanate interfaces with a polar perovskite, such as LaAlO$_3$, it has been suggested [28] that oxygen vacancies (OV)

create magnetic moments through orbital reconstruction and e_g occupancy, thereby modifying the occupied electronic levels produced by the so-called polar catastrophe. Oxygen-deficient STO in bulk has been discovered to contain optically induced magnetic moments [15], and the magnetism inverts sign upon switching between right- and left-circular polarization. Recently, a spin- and angle-resolved photoemission spectroscopy (SARPES) study [16] has shown that the concentric circular bands have a gap at the Γ point, opposite spin chirality, and a large value of split at the Fermi surface that cannot be explained by a purely Rashba-like model. It was suggested that this state breaks time-reversal symmetry [16], and an argument in favor of an antiferromagnetic ground state as the result of one of the instabilities of the 2D Fermi liquid with exchange interactions has been presented [29].

II. GOALS AND MAIN RESULTS

In this paper, through a relaxed spin-unconstrained density functional theory (DFT) study of (001) terminated STO slabs with various surface oxygen vacancy patterns, we show that stable periodic arrays of oxygen vacancies can form in a surface TiO$_2$ layer and cause the spin degeneracy of the occupied subbands to be lifted at the generalized gradient approximation (GGA) level giving rise to a weakly ferromagnetic ground state. By considering slabs with multiple surface oxygen vacancy configurations (such as those of Fig. 1 and those discussed in Appendix A) and various surface OV densities n_v (= 1/4, 1/6, and 1/8), we find that for a given surface OV density, the superstructure in which the surface oxygen vacancies order in periodic stripe arrays, such as the one in Fig. 1, is characterized by the lowest energy. In addition, Fig. 2 shows the particular stripe-ordered vacancy configuration which is the most stable within an allowed range of oxygen chemical potential. Furthermore, the Ti atoms of the top layer and the layer just below it acquire stable magnetic moments below surface OV density of $n_v = 1/8$ (Table I) producing an internal Zeeman field, in which the level of doping and the surface magnetic moments are functions of surface OV density. At the Γ point, the Q2DEG is spread over multiple layers

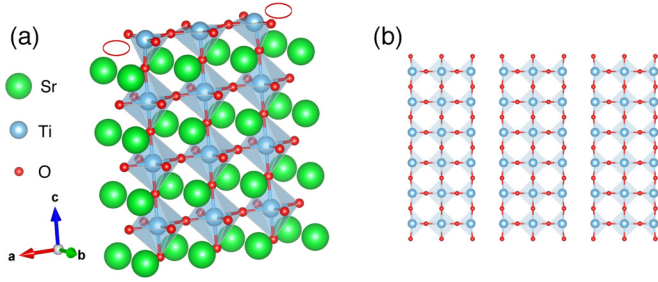---

*Corresponding author: manousakis@gmail.com

FIG. 1. (a) Four layers of atomically relaxed STO bounded in the (001) direction by an SrO surface on one side and a TiO$_2$ surface on the other side forming a 3×1 supercell with an imposed 1/6 surface OV coverage in a stripe configuration. The presence of the oxygen vacancies (the sites of which are denoted by the two red circles) cause the tetrahedra at the TiO$_2$ surface to buckle and push both the O and the Ti atoms away from the lower layers. The Ti-Ti bond length at the surface is larger by about 0.3 Å along the x axis as compared to that along the y axis. (b) Top surface head-on view of the superlattice structure of oxygen vacancy ordering in periodic arrays.

and hosted by spin-nondegenerate states several hundred meV below the Fermi level. These deeper occupied states near the zone center, which are strongly $3d_{xy}$ in character, host a Q2DEG but contribute a relatively small part to the net magnetic moment, most of which is localized on the Ti atoms at the oxygen-deficient surface away from the zone center, and hosted by a reconstructed mixture of t_{2g} and e_g. Last, these findings via *ab initio* calculations are strongly supported by the following results. Taking into account a Rashba interaction in the x-y plane, we find that these spin-split bands near the zone center acquire the spin-momentum correlations recently discovered [16] by a SARPES study. The zone center gap
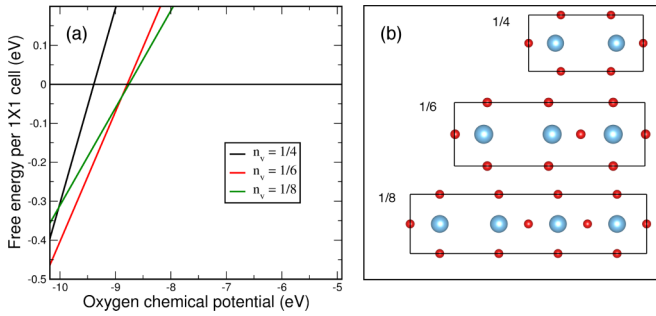

FIG. 2. (a) Stability graph of the striped vacancy pattern discussed in Fig. 1 with different surface OV densities. All three densities produce similar subsurface $3d_{xy}$ bands near the zone center but differ in the magnitude of the magnetic moments. For an explanation of the free energy and the allowed range of oxygen chemical potential see Appendix F. (b) Top view of the various Ti$_{(m)}$O$_{(n)}$ units at the TiO$_2$ surface with one oxygen vacancy per unit cell (u.c.), showing (i) a 2×1 u.c. with one eliminated O atom at (0.50,0.50) creating a stripe of missing oxygen atoms along the y axis (OV surface density $n_v = 1/4$) and giving each Ti atom exactly one nearest neighbor vacancy, (ii) a 3×1 u.c. with one eliminated O at (0.33,0.50) causing a similar vacancy stripe but with lower density ($n_v = 1/6$), and (iii) a 4×1 u.c. with one eliminated O at (0.25,0.50), creating vacancy stripes with an OV surface density of $n_v = 1/8$. Further vacancy configurations are discussed in Appendix A.

TABLE I. Magnetic moments of surface Ti atoms and of those one layer below the surface, in units of μ_B. For $n_v = 1/6$, Ti(1) refers to the atom closest to the O vacancy, and Ti(2) refers to the atom farther away. The configurations not shown in Fig. 1 have been discussed in Appendix A.

	1/4	1/6, Ti(1)	1/6, Ti(2)	1/8	Dimer	2×1
Surface layer	0.371	0.142	0.264	0.000	0.367	0.000
Second layer	0.023	0.053	0.118	0.000	0.047	0.000

is enhanced by the introduction of a Coulomb U term via a GGA $+$ U calculation, but the qualitative features of the spin chirality and the momentum-spin correlations of the bands in the direction parallel to the surface, as well as the bands themselves near the Γ point are reproduced. The spin chirality perpendicular to the surface is attributed to a matrix element of the SARPES process [16,30].

III. COMPUTATIONAL DETAILS

We consider slabs between four and six STO layers thick, terminated in the (001) direction by an SrO surface on one end and an oxygen-deficient TiO$_2$ surface on the other.

We used at least 15 Å of vacuum between repeated images in the (001) direction to minimize dipole interaction. The presence of surfaces in the (001) direction of our slab geometry creates an electrostatic confinement potential well which has one minima near the oxygen-deficient TiO$_2$ surface, and another near the TiO$_2$ layer on the opposite (SrO surface) end. This gives rise to low energy bound states close to both surfaces. We focus on the dispersive bands localized close to the oxygen-deficient TiO$_2$ surface and within the depth range of the ARPES study.

All computations were performed using the plane-wave basis set (plane-wave cutoff of 540 eV) with the projector augmented wave (PAW) methodology [31] used to describe the wave functions of the core electrons, as implemented in the VASP package [32–35]. The Perdew-Burke-Ernzerhof (PBE) exchange-correlation functional [36] was used for all GGA calculations. The $4s,4p,5s$ electrons of the Sr, the $4s,3d,3p$ electrons of the transition-metal atom, and the $2s,2p$ electrons of the oxygen were treated as valence electrons. We checked our results for consistency by including the semicore s states of the Ti atom as valence states, which caused a negligibly small increase of the Ti magnetic moments by a maximum of $0.005\mu_B$ in ferromagnetic supercells.

The asymmetry of the slab allows us to disregard interactions between vacancies and to model a real slab with inequivalent surfaces on either side, at the cost of introducing a net dipole moment and an artificial field induced in the vacuum region. We compensated for this effect using internal VASP dipole correction routines, and found a correction to the *total energy* of a supercell of 59 atoms and 474 electrons to be only $\sim$30 meV. The smallness of the correction is due to the STO's high polarizability [25] and the neutrality of its SrO and TiO$_2$ planes, making the dipole corrected results accurate.

An initial unit cell length of 3.944 Å was used, which was found by curve-fitting the ground state energies of bulk STO to find the minimum. This value is about 1% higher than

room temperature bulk-STO cubic phase value (3.905 Å). The Brillouin zone was sampled with a maximum of $5 \times 15 \times 1$ k-point mesh for the self-consistent cycles [37]. Forces were converged to less than 10 meV/Å for each ion. Local Coulomb repulsion of Ti $3d$ electrons was accounted for within GGA + U approach with $U_{Ti} = 2$ eV [38]. The PBE functional and the PAW potentials reproduce fairly well the bulk behavior of STO in the cubic phase and in the antiferrodistortive (AFD) tetragonal phase while being limited to the accuracy of the PAW PBE methodology. The nature of the Ti d bands in bulk are correctly reproduced although the gap is underestimated (2.1 eV in PBE as opposed to 3.2 eV experimental value). In the cubic phase, we found an expected instability through frozen phonon calculations in the form of an imaginary soft phonon mode, and in the tetragonal phase, we see the expected octahedra rotations. Both these observations agree quantitatively with existing literature [39].

IV. *AB INITIO* CALCULATIONS

The Q2DEG in STO has been associated with a band bending of ~ 300 meV near the surface [13,17]. Confinement in this potential well lifts the degeneracy between the $3d_{xy}$ of different Ti atoms and replaces the smooth k_z dependence in bulk by a discrete series of light parabolic subbands split in energy. The number of parabolic subbands scales with the number of TiO$_2$ layers in the slab. Oxygen vacancy doping lifts the spin degeneracy in each of these bands but by different magnitudes, as shown in Fig. 3.

We would like to discuss the stability of our proposed OV ordering configuration to the other competing OV ordering configurations considered in Appendix A. In particular, the $\sqrt{2} \times \sqrt{2}$ configuration shown in Fig. 7 has been proposed to be the actual oxygen-deficient STO surface reconstruction

FIG. 3. The near-Γ spin-GGA band structure of the four STO layer with striped vacancy configuration ($n_v = 1/6$). Up-spin bands are denoted with solid lines and corresponding down-spin bands are denoted with dashed lines. The $3d_{xy}$ bands are light and dispersive, while the $3d_{xz}$ and the $3d_{yz}$ are heavier and less dispersive due to confinement in the z direction, which also produces the observed level quantization of states.

in a paper (Ref. [40]) which became publicly available after submitting our present work for publication. The stripe configurations are lower in energy by ~ 0.2 eV (for $n_v = 1/4$) per supercell used in the DFT calculations than the nonstripe configurations shown in Appendix A. One, however, might ask, what happens when one allows for the AFD distortion found in the $\sqrt{2} \times \sqrt{2}$ configuration to coexist together with the stripe. Will the two ordering effects, i.e., the stripe ordering and the AFD ordering, compete or will they coexist? The above-mentioned energy gain by forming the stripe order is an order of magnitude higher than the internal energy difference between the cubic and the AFD phase as calculated by *ab initio* methods [39,41–43] in bulk. Thus, there is no competition between the two forms of order due to a much larger gain in energy by forming the stripe order; in addition, these two orders are not frustrating each other. Therefore, we expect the stripe order to occur at much higher temperature than the transition to the AFD phase.

For each of the four, five, and six STO-layer slabs and for stripe ordering of vacancies, we find that there are multiple spin pair bands (see Figs. 3 and also Fig. 8 in Appendix B) at the GGA level below the Fermi level. A question arises as to why ARPES observes [14,16] only one light subband pair. The answer to that lies in the fact that only the lowest two spin pairs of subbands are significantly bound to Ti atoms close to each surface, and only one out of those two pairs is localized strongly near the TiO$_2$ surface on which ARPES measurements are taken. We illustrate this using a site and Y_{lm} projection (Fig. 9 in Appendix C). This is a consequence of the fact that the surface potential creates bound states. The higher subbands are more delocalized and have a weaker surface contribution. Furthermore, as we illustrate in Appendix C (Fig. 10), the addition of an on-site Hubbard Coulomb-U term causes the electrons to repel each other and move away from the surface, leaving all but one pair strongly within the range of the ARPES probe. Keeping this picture in mind, We find that four STO-layer and six STO-layer slabs have qualitatively similar band structure (see Fig. 8 in Appendix B), hence we believe that our results and conclusions presented here, which are obtained from slabs containing only four STO layers and 1/6 surface OV density (Fig. 1) may be applicable to the infinite-slab-thickness limit. The pair of bands associated with atoms near the TiO$_2$ surface has a zone-center splitting of ~ 48 meV at the GGA level and ~ 70 meV at the GGA + U ($U = 2$ eV) level. Around the Γ point, they are all $3d_{xy}$, except the heavy subbands ~ 50 meV below the Fermi surface, which are largely $3d_{xz}$. The nature of these $3d$ bands is identical to those in DFT calculations with symmetric slabs, further validating our use of asymmetric slabs.

By switching on the spin-orbit coupling (SOC) in the system, we find a slightly modified near-Γ band structure for the four STO-layer slab, as shown in Appendix D, Fig. 11. The change in the $3d_{xy}$ bands around the Γ point is negligible. The biggest effect of SOC can be seen in lifting the degeneracy of the band- crossing at the corners, as expected. It preserves the net magnetic moment at the surface and the spin -polarization of the $3d_{xy}$ bands around the Γ point. At this mean-field level, SOC effect is predictably small enough so that the spin-orbit mixing changes the spin- eigenstates only by a small amount and the spin up-down characterization remains
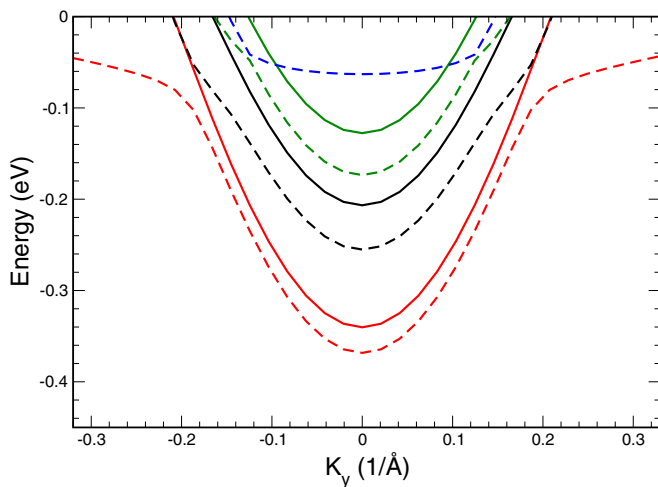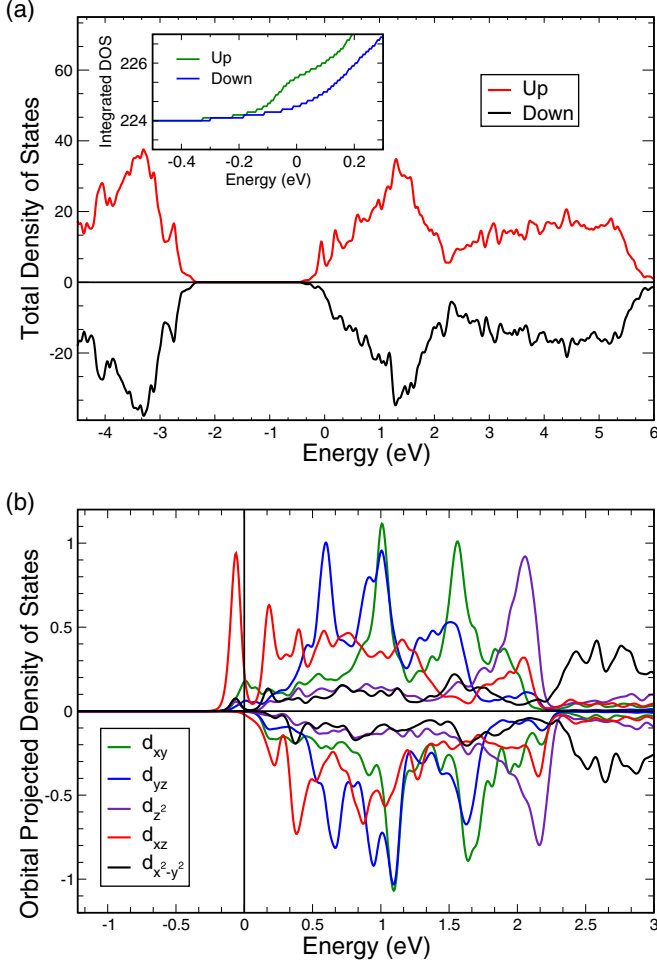
(a)

(b)

FIG. 4. (a) Total up and down DOS of a four STO-layer slab with 1/6 OV surface density at the TiO$_2$ surface. The zero is the Fermi level at the present level of doping. Inset: Integrated up and down DOS, showing the onset of magnetism at $\sim$300 meV below the Fermi level. (b) Projected DOS of the 3d orbitals of a surface Ti atom next to an oxygen vacancy. The occupied polarized states are a mixture of spin-polarized t_{2g} and e_g located around the S point of the BZ.

valid. The most important role of the spin-orbit coupling is that it simply selects the direction of the effective internal "Zeeman field" (which splits our lowest energy bands within our GGA-spin calculation) to be perpendicular to the orbital angular momentum x-y plane.

Figure 4 shows the total density of states (DOS) of a four STO-layer slab along with the integrated up and down DOS as a function of energy as well as the orbital projected DOS of one of the Ti atoms at the surface at the GGA level. We find that in the absence of a Rashba term and at 1/6 OV surface density, the low-lying 3d_{xy} bands near the zone center carry finite but small amounts of magnetic moments. Most of the contribution to the magnetic moment comes from heavier subbands away from the zone center, and depend on a reconstruction of the e_g states. As we can observe in Fig. 4, the spin-polarized e_g states of the Ti atom next to a missing oxygen is pulled below the Fermi level and get mixed with the t_{2g} states. On the other hand, the occupied bands of the Ti atoms one layer below the

surface are entirely t_{2g} in nature with almost nonmagnetic 3d_{xy} states (refer to Appendix E, Fig. 12).

The splitting of the e_g states and their mixing with the t_{2g} states give the surface Ti atoms a magnetic moment (with magnetic moments for the two nonequivalent surface Ti atoms given by $M_{\mathrm{Ti}^{(1)}} = 0.142\mu_{\mathrm{B}}$ and $M_{\mathrm{Ti}^{(2)}} = 0.264\mu_{\mathrm{B}}$) each for $n_v = 1/6$.

V. INCLUSION OF THE RASHBA COUPLING

The band picture shown in Fig. 3 does not take into consideration the Rashba effect, which couples spin with momentum. In the existence of strong fields caused by surface termination and oxygen vacancy, inversion symmetry is lost and the octahedra buckle, causing previously forbidden hopping channels to open. This, coupled with a strong spin-orbit coupling [26] produces a prominent planar Rashba effect. For the band pair localized on the Ti atom one unit cell below the oxygen-deficient surface, this effect can be modeled using a simple two-dimensional Hamiltonian for small values of **k**. Written in the basis of Ti 3d_{xy} Bloch states and S_z eigenstates, the Hamiltonian is

$$\hat{H} = \epsilon_{\mathrm{GGA}}(\vec{k})\hat{\mathrm{I}} - \alpha(\sigma_x k_y - \sigma_y k_x) - h\sigma_z, \quad (1)$$

where α is the Rashba parameter, σ_x, σ_y, and σ_z are Pauli matrices, and $\hat{\mathrm{I}}$ is the unit matrix. The last term is the Zeeman term due to an effective internal mean field in the z direction which is responsible for the spin splitting of the bands found by allowing for spin and lattice relaxation within the GGA and GGA $+ U$. In the absence of an external magnetic field, both magnetic directions along the z axis are equally likely, and we use $h = \pm|h|$ to account for ferromagnetic domains that average to zero in a macroscopic measurement like SARPES [16]. Here $\epsilon_{\mathrm{GGA}}(\vec{k})$ is the band structure obtained as the average between the lowest two near-surface subbands close to the oxygen-deficient TiO$_2$ surface obtained in our DFT calculation which correspond to spin-up and spin-down states, and the value of this field will be chosen to reproduce the energy splitting of these two lowest bands. In addition, $\epsilon_{\mathrm{GGA}}(\vec{k})$ is very close (apart from a constant) to the results of our DFT calculation when we do not include spin. The eigenvalues of this Hamiltonian are

$$e_{\pm}(k) = \epsilon_{\mathrm{GGA}}(\vec{k}) \pm |h|\Delta(k); \qquad \Delta(k) = \sqrt{1 + \gamma^2 k^2}, \quad (2)$$

where $k^2 = k_x^2 + k_y^2$ and $\gamma = \alpha/|h|$. The corresponding expectation values of the spin components are as follows:

$$\begin{pmatrix} \langle\pm|\sigma_x|\pm\rangle \\ \langle\pm|\sigma_y|\pm\rangle \\ \langle\pm|\sigma_z|\pm\rangle \end{pmatrix} = \mp\frac{1}{\Delta(k)}\begin{pmatrix} \gamma k_y \\ -\gamma k_x \\ \frac{h}{|h|} \end{pmatrix}. \quad (3)$$

In Fig. 5 we compare the experimentally determined bands to the bands located on the TiO$_2$ layer immediately next to the oxygen-deficient surface and obtained using Eq. (2) by choosing the parameters in the following way. Figure 5(a) shows the result of our fit of the experimentally determined x component of the spin to the form given by Eq. (3) where the only fitting parameter is γ. The solid line is the result of our fit with $\gamma = 17.045$ Å. Figure 5(b) is obtained using $h = 24.2$ meV as found by our spin GGA calculation and the
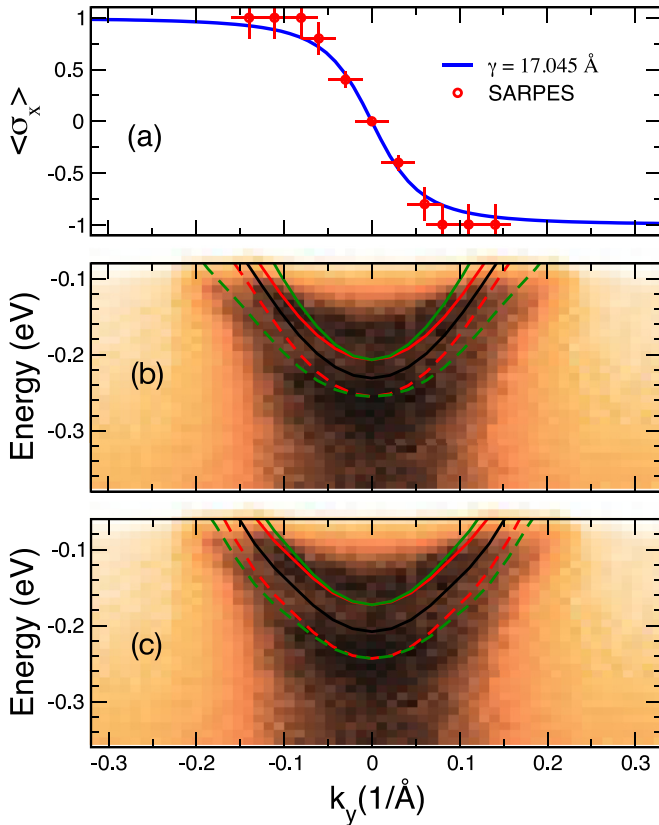
FIG. 5. (a) The result of fitting the experimentally determined [16] spin x component via a chi-square fit to the form given by Eq. (3) indicating a large planar Rashba coupling near the surface. (b) The spin pair of near-surface GGA bands of the four STO-layer slab after applying a Rashba spin-split term using Eq. (2) as compared to the experimental results [16]. Other occupied d_{xy} bands are deeper inside the slab and are omitted in this figure. (c) The same as in (b) using the bands by GGA + U. The black solid line is the result of GGA or GGA + U without spin relaxation. The green and red solid (dashed) lines are obtained with GGA or GGA + U after spin relaxation for down (up) with and without the Rashba interaction, respectively.

value of $\gamma = 17.045$ Å determined by the previously discussed fit. This implies that the Rashba parameter is 412 meV Å for the given value of h.

Figure 5(c) is obtained using $h = 35.5$ meV as found in GGA + U calculation for a four STO-layer slab and $\alpha = 300$ meV Å, illustrating a better agreement of the zone-center gap and the momentum dispersion of the bands with experiment.

We note that there is a possibility that SARPES overestimates the spin polarization by not accurately estimating the quasiparticle spectral weight away from the peak of the spectral function: it is clear that the quasiparticle function is widely spread around the peak, and thus the part of the spectral weight away from the peak can hide under the contribution of tails from other nearby bands. In such case the estimation of the Rashba parameter can be significantly affected.

The photoexcitation process itself mixes states with different angular momentum components, which depend on the light polarization, causing a rotation of the electron spin polarization

through the spin-orbit coupling term. Thus, the expectation value $\langle \sigma_z \rangle$ picks up a contribution proportional to $\langle \sigma_x \rangle$ and/or to $\langle \sigma_y \rangle$. In the absence of an external magnetic field, the average value of the term proportional to h over the entire surface is expected to be zero. This can explain why the expectation value of $\langle \sigma_z \rangle$ measured in the SARPES study has a k dependence similar to that of $\langle \sigma_x \rangle$ or $\langle \sigma_y \rangle$.

VI. CONCLUSIONS

In conclusion, we find that our *ab initio* calculations predict very interesting patterns of OV ordering on the (001) STO surface which lead to a small ferromagnetic moment of the surface Ti atoms. Furthermore, major experimental characteristics of the STO surface can be qualitatively reproduced by a GGA (and GGA + U) spin calculation where we have included the effects of the planar Rashba coupling. The underlying symmetry breaking and the presence of a quantum-well potential near the surface give rise to discrete energy bands in the (001) direction. When surface oxygen vacancies are introduced and the structure is relaxed within a spin-dependent GGA, bands near the TiO_2 surface emerge characterized by a dispersion near the zone center similar to that observed by recent SARPES studies. More importantly, we find that the fully relaxed GGA calculation opens a spin gap at the zone center, which is further enhanced by adding a moderate U in a GGA + U calculation. The contribution to the magnetic moments comes primarily from the neighborhood of the S and X points in the BZ, and localized at the reconstructed t_{2g} and e_g of the Ti atoms at the oxygen-deficient surface (Fig. 6). At the spin-GGA level and at the present high levels of doping, the system is weakly ferromagnetic. Therefore, it is reasonable to assume a theoretical framework whereby we identify with
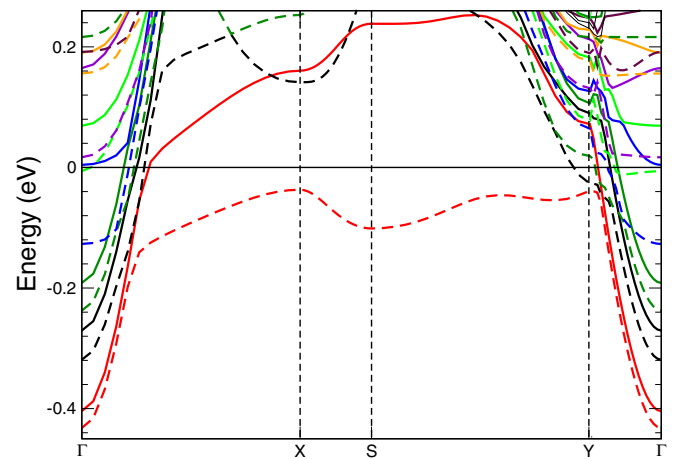

FIG. 6. The planar BZ band structure of the oxygen-deficient four STO-layer slab with $n_v = 1/6$. Up spins are denoted with solid lines and down spins are denoted with dashed lines. The lowest occupied pair of spin bands is degenerate near the Γ point and is contributed by the Ti atoms away from the oxygen-deficient TiO_2 surface. The second lowest spin-split pair comes from the Ti atoms one pair below the oxygen-deficient TiO_2 surface, which are the bands of interest. The majority of the magnetic moment comes from the BZ corner and edge where the states are localized on the doped TiO_2 surface as a mixture of t_{2g} and e_g with a considerable spin split.

these $3d_{xy}$ bands those seen in the most recent SARPES study [16]. Then by taking these bands as a starting point we turned on a planar Rashba term, the lowest lying, closest to the TiO$_2$ surface $3d_{xy}$ bands qualitatively reproduce the experimental SARPES results [16] for the energy bands close to the Γ point. Furthermore, they reproduce the momentum-spin correlations in the x and y directions seen in SARPES and they have no net magnetic moment in the x-y plane.

ACKNOWLEDGMENTS

APPENDIX A: OTHER VACANCY CONFIGURATIONS

Figure 7 shows the vacancy configurations considered here which are not shown in the main part of the paper associated with Fig. 1.

The (1/4) stripe and dimer configurations have stable magnetic moments at the spin-GGA level, while the (1/8) stripe and 2×1 configurations have no noticeable magnetic moments. In Table I we list the magnetic moments of the surface and subsurface Ti atoms for all the systems under consideration. For the stripe configuration with $n_v = 1/4$, the two surface Ti atoms have similar environment and equal magnetic moments. For $n_v = 1/6$, the Ti atoms next to the OV has less magnetic moment than the Ti with all nearest-neighbor oxygen atoms present.

APPENDIX B: THE INFINITE SLAB-THICKNESS LIMIT

In bulk SrTiO$_3$, the conduction d-bands have a smooth k_z dependence and are made out of a superposition of states from every Ti atom. In a (001) slab of thickness L, the k_z vector does not exist, and the dispersive Bloch band is replaced by a series of bands with different Γ-point energies. Each of these
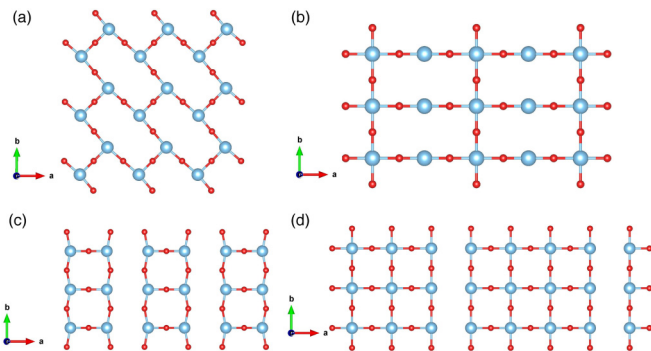

FIG. 7. (a) A four STO-layer slab with $\sqrt{2} \times \sqrt{2}$ (dimerized) vacancies, causing each surface Ti to have one nearest-neighbor vacancy. (b) A 2×1 configuration with chains of vacancies in the y direction. The configuration (b) contains two different types of surface Ti: one with no nearest-neighbor vacancies, and the other with two nearest-neighbor vacancies. Both configurations have doping level $n_v = 1/4$ (25%). (c) Stripe configuration, $n_v = 1/4$ and (d) stripe configuration, $n_v = 1/8$.
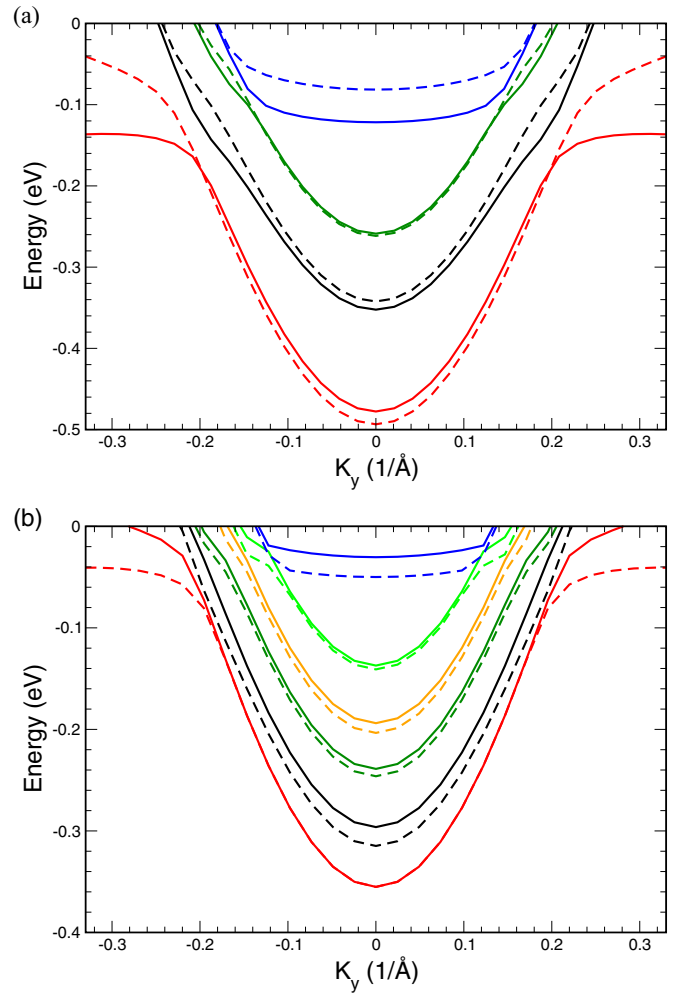

FIG. 8. Comparison of the near zone-center conduction bands of oxygen-deficient (a) four-layer STO and (b) six-layer STO with $n_v = 1/4$. Up-spin bands are denoted by solid lines and down-spin bands by corresponding dashed lines. The spin split is maximum for the bands near the OV surface and reduces as we go deeper into the bulk.

subbands now have unequal contribution from each Ti atom depending on the atom's z index. There will be quantum wells of noticeable depth at the TiO$_2$ surface and at the SrO surface with bound states in each. These states are found to have the lowest energy and the wave functions corresponding to them will decay exponentially outside the wells with characteristic length scales ξ and χ, respectively. As we change the slab thickness, as long as $\xi \ll L$ and $\chi \ll L$, the finite-size effect of these bound surface states will be exponentially small. However, the other subband states unbound to the surface potential wells will be affected no matter how big L is because the wave functions always vary over a distance L. Therefore, in our problem we expect two types of states. Those bound states which have weak finite-size effects and those unbound states which no matter how big L is, they will continually change until they form a continuum which will give rise to the (001) dependence of the bands in the bulk limit.

This is almost exactly what we find in our study. Figure 8 shows the near zone-center bands of a four STO-layer and a six STO-layer slab for $n_v = 1/4$. The lowest two spin pairs
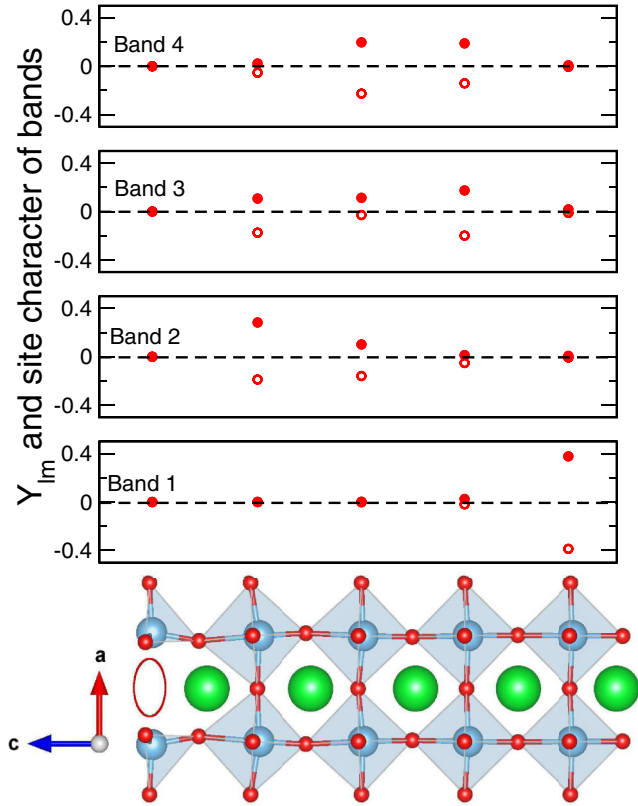
FIG. 9. Orbital and site projection of the lowest four spin pairs of bands of a five STO-layer slab ($n_v = 1/4$) around the Γ point and along k_y, with band 1 being the deepest pair. The site locations are shown by the crystal unit cell aligned along the horizontal axis. On the graph, red is d_{xy} and green is d_{xz}. Up spin is above the axis and is shown in filled circles, whereas down spin is below the axis and is shown in empty circles. The position of the missing oxygen on the surface is shown with a red circle. Each d_{xy} subband can be seen to prefer different TiO$_2$ planes. The deepest pair of bands is the Ti d_{xy} near the SrO surface and the next deepest pair is Ti d_{xy} next to the TiO$_2$ surface. They are the bound states and are the most localized.

FIG. 10. Orbital and site projection of the lowest four spin pairs of bands of a five STO-layer slab ($n_v = 1/4$) around the Γ point and along k_y, with band 1 being the deepest pair. A GGA + U scheme has been used. The site locations are shown by the crystal unit cell aligned along the horizontal axis. On the graph, red is d_{xy} and green is d_{xz}. The position of a missing oxygen on the surface is shown with a red circle. The Coulomb term causes the spins in a pair to move away from each other in real space, but the quantization effect of the confining potential is maintained. Up spin is above the axis and is shown in filled circles, whereas down spin is below the axis and is shown in empty circles.

correspond to the bound states close to the SrO and the TiO$_2$ surface, respectively, in both cases and the impact of the slab thickness on them is minimal. The six STO-layer slab has more subbands of d_{xy} character unbound to either surface wells, but most of these are away from the depth range of SARPES (as demonstrated in Fig. 9 for five STO-layer slabs), and the band structure near the Fermi level near the surface is the same between the four and six STO-layer slabs. We therefore believe that the results obtained from four STO-layer-thick slabs may be valid for the infinite slab-thickness limit.

APPENDIX C: ORBITAL AND SITE-PROJECTION OF BANDS

In Fig. 9 the orbital and site projection of the lowest four spin pairs of bands around the Γ point and along k_y for the five STO-layer slab with $n_v = 1/4$ at the GGA level is illustrated with band 1 being the deepest pair. The colors signify the orbital character of the band (red = d_{xy}, green = d_{xz}) and the unit cell along the horizontal axis is a reference to the Ti site
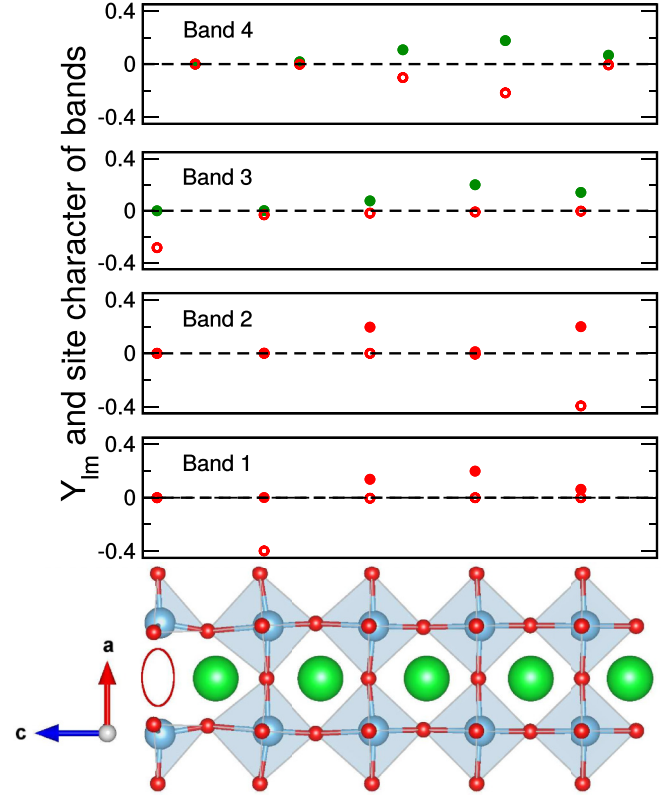
location of these states inside the unit cell. One spin pair is seen to have the most localization near the TiO$_2$ surface and is the experimental surface band pair. However, some surface contribution from the next pair of subbands is also visible. A Coulomb U in the form of GGA + U repels the spins from one another in real space and causes the spin pairs to spread, as a result of which the up-spin and the down-spin bands are nested on neighboring Ti atoms, there are fewer bands near the TiO$_2$ surface, and the spin gap is widened. We demonstrate this in Fig. 10 which illustrates the near-Γ orbital and site projection of the deepest corresponding occupied bands around the Γ-point for a five STO-layer slab ($n_v = 1/4$) (using $U = 4$ eV and $J = 1$ eV).

APPENDIX D: SPIN-ORBIT COUPLING

In Fig. 11 we give the results obtained by switching on the SOC in a four STO-layer slab with $n_v = 1/4$. As can be seen, we get a slightly modified near-Γ band structure as compared to Fig. 8 where the SOC was neglected. The effect of SOC is
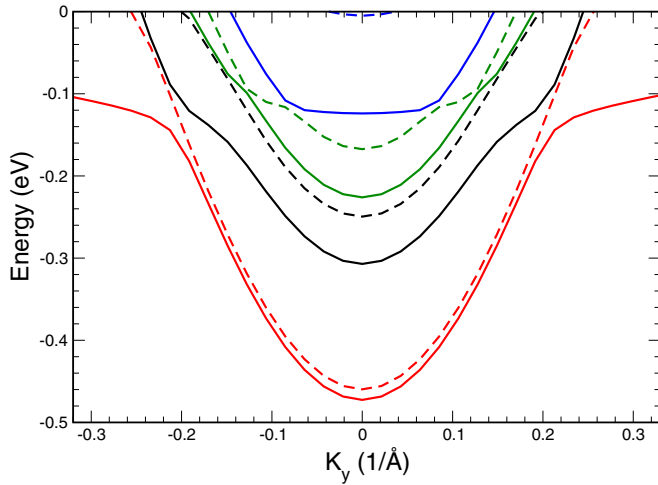
FIG. 11. The near-Γ band structure of the oxygen-deficient four-layer STO ($n_v = 1/6$) with spin-orbit coupling included. Up spins are denoted with solid lines and down spins are denoted with dashed lines. The change in the d_{xy} bands close to the Γ point is negligible. The biggest effect of SOC can be seen in lifting the degeneracy of the band crossing at the corners.
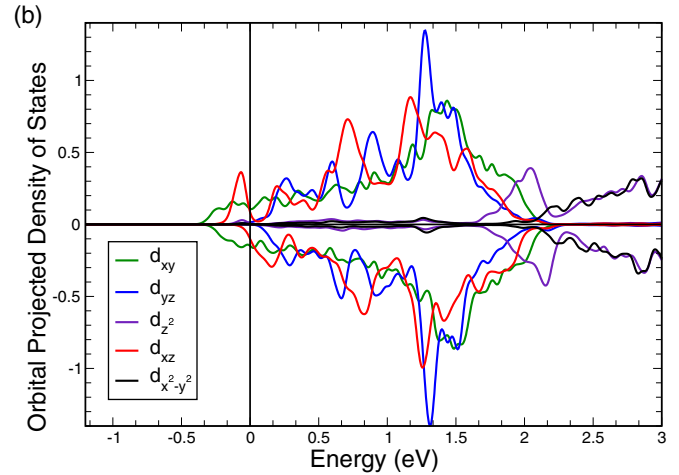

FIG. 12. DOS of the $3d$ states of a Ti atom one layer below the oxygen-deficient TiO$_2$ surface ($n_v = 1/6$). The occupied states around the zone center are t_{2g} in nature. At this GGA level, the d_{xy} states carry negligible magnetic moments, and most of the spin polarization is in the d_{xz} state.

found to be maximum where the bands cross each other, as expected. It preserves the net magnetic moment at the surface and the spin polarization of the d_{xy} bands around the Γ point.

APPENDIX E: DENSITY OF STATES OF THE Ti ATOM ONE LAYER BELOW THE SURFACE

In contrast to the surface Ti atoms whose occupied states are a mix of t_{2g} and e_g, the projected density of states in the Ti atom one layer below the surface (Fig. 12) with $n_v = 1/6$ shows far less polarization, with its occupied states being predominantly t_{2g} in character and located near the zone center. Here the magnetic moment is an order of magnitude less than that on the surface, and most of the polarization is in the d_{xz} state.

APPENDIX F: STABILITY OF OXYGEN VACANCIES

The possible range of oxygen chemical potential μ_0 can be determined by first noting that the value is bounded from above by the chemical potential of the triplet O$_2$ molecule,

$$\mu_O < \mu_{O_2}/2 = -4.917 \text{ eV}. \quad \text{(F1)}$$

Furthermore, it is constrained by the relation

$$\mu_{Sr} + \mu_{Ti} + 3\mu_O = \mu_{SrTiO_3}^{bulk} = -40.125 \text{ eV}, \quad \text{(F2)}$$

where the chemical potentials of Sr and Ti must themselves satisfy inequality constraints:

$$\mu_{Sr} < \mu_{Sr}^{bulk} = -1.6840 \text{ eV}, \quad \text{(F3)}$$

$$\mu_{Ti} < \mu_{Ti}^{bulk} = -7.8981 \text{ eV}. \quad \text{(F4)}$$

Therefore the allowable energy of the oxygen chemical potential is

$$-10.181 \text{ eV} < \mu_O < -4.917 \text{ eV}. \quad \text{(F5)}$$

The free energy per unit cell plotted in Fig. 2 for each oxygen-deficient structure is taken to be

$$F = [F_V - F_0 + \mu_0]/N_u, \quad \text{(F6)}$$

where F_V is the free energy of the oxygen-deficient structure, F_0 is the free energy of the no-vacancy structure, and N_u is the number of 1×1 unit cells needed to make the supercell used in our DFT.

All three structures are stable at only very low oxygen chemical potential in equilibrium. Therefore, we believe that nonequilibrium effects like intense UV irradiation are necessary to create oxygen vacancies with the density required for the spin split.

[1] A. Ohtomo and H. Y. Hwang, Nature (London) **427**, 423 (2004).

[2] H. Y. Hwang, Y. Iwasa, M. Kawasaki, B. Keimer, N. Nagaosa, and Y. Tokura, Nat. Mater. **11**, 103 (2012).

[3] C. Cen, S. Thiel, G. Hammerl, C. W. Schneider, K. E. Andersen, C. S. Hellberg, J. Mannhart, and J. Levy, Nat. Mater. **7**, 298 (2008).

[4] J. Mannhart and D. G. Schlom, Science **327**, 1607 (2010).

[5] S. Thiel, G. Hammerl, A. Schmehl, C. W. Schneider, and J. Mannhart, Science **313**, 1942 (2006).

[6] K. Ueno, S. Nakamura, H. Shimotani, A. Ohtomo, N. Kimura, T. Nojima, H. Aoki, Y. Iwasa, and M. Kawasaki, Nat. Mater. **7**, 855 (2008).

[7] A. Brinkman, M. Huijben, M. van Zalk, J. Huijben, U. Zeitler, J. C. Maan, W. G. van der Wiel, G. Rijnders, D. H. A. Blank, and H. Hilgenkamp, Nat. Mater. **6**, 493 (2007).

[8] N. Reyren, S. Thiel, A. D. Caviglia, L. F. Kourkoutis, G. Hammerl, C. Richter, C. W. Schneider, T. Kopp, A.-S. Retschi, D. Jaccard, M. Gabay, D. A. Muller, J.-M. Triscone, and J. Mannhart, Science **317**, 1196 (2007).

[9] L. Li, C. Richter, J. Mannhart, and R. C. Ashoori, Nat. Phys. **7**, 762 (2011).

[10] J. A. Bert, B. Kalisky, C. Bell, M. Kim, Y. Hikita, H. Y. Hwang, and K. A. Moler, Nat. Phys. **7**, 767 (2011).

[11] A. P. Ramirez, Science **315**, 1377 (2007).

[12] C. Cen, S. Thiel, J. Mannhart, and J. Levy, Science **323**, 1026 (2009).

[13] A. F. Santander-Syro, O. Copie, T. Kondo, F. Fortuna, S. Pailhes, R. Weht, X. G. Qiu, F. Bertran, A. Nicolaou, A. Taleb-Ibrahimi, P. Le Fevre, G. Herranz, M. Bibes, N. Reyren, Y. Apertet, P. Lecoeur, A. Barthelemy, and M. J. Rozenberg, Nature (London) **469**, 189 (2011).

[14] N. C. Plumb, M. Salluzzo, E. Razzoli, M. Månsson, M. Falub, J. Krempasky, C. E. Matt, J. Chang, M. Schulte, J. Braun, H. Ebert, J. Minár, B. Delley, K.-J. Zhou, T. Schmitt, M. Shi, J. Mesot, L. Patthey, and M. Radović, Phys. Rev. Lett. **113**, 086801 (2014).

[15] W. A. D. Rice, P. Ambwani, M. Bombeck, J. D. Thompson, G. Haugstad, C. Leighton, and S. A. A. Crooker, Nat. Mater. **13**, 481 (2014).

[16] A. F. Santander-Syro, F. Fortuna, C. Bareille, T. C. Rödel, G. Landolt, N. C. Plumb, J. H. Dil, and M. Radovic, Nat. Mater. **13**, 1085 (2014).

[17] W. Meevasana, P. D. C. King, R. H. He, S.-K. Mo, M. Hashimoto, A. Tamai, P. Songsiririthigul, F. Baumberger, and Z.-X. Shen, Nat. Mater. **10**, 114 (2011).

[18] Y. Lee, C. Clement, J. Hellerstedt, J. Kinney, L. Kinnischtzke, X. Leng, S. D. Snyder, and A. M. Goldman, Phys. Rev. Lett. **106**, 136809 (2011).

[19] M. Kim, C. Bell, Y. Kozuka, M. Kurita, Y. Hikita, and H. Y. Hwang, Phys. Rev. Lett. **107**, 106801 (2011).

[20] Y. Kozuka, M. Kim, C. Bell, B. G. Kim, Y. Hikita, and H. Y. Hwang, Nature (London) **462**, 487 (2009).

[21] Y. Kozuka, M. Kim, H. Ohta, Y. Hikita, C. Bell, and H. Y. Hwang, Appl. Phys. Lett. **97**, 222115 (2010).

[22] B. Jalan, S. Stemmer, S. Mack, and S. J. Allen, Phys. Rev. B **82**, 081103 (2010).

[23] J. Shen, H. Lee, R. Valentí, and H. O. Jeschke, Phys. Rev. B **86**, 195119 (2012).

[24] Z. S. Popović, S. Satpathy, and R. M. Martin, Phys. Rev. Lett. **101**, 256801 (2008).

[25] G. Khalsa and A. H. MacDonald, Phys. Rev. B **86**, 125121 (2012).

[26] G. Khalsa, B. Lee, and A. H. MacDonald, Phys. Rev. B **88**, 041302 (2013).

[27] Y. J. Chang, L. Moreschini, A. Bostwick, G. A. Gaines, Y. S. Kim, A. L. Walter, B. Freelon, A. Tebano, K. Horn, and E. Rotenberg, Phys. Rev. Lett. **111**, 126401 (2013).

[28] N. Pavlenko, T. Kopp, and J. Mannhart, Phys. Rev. B **88**, 201104 (2013).

[29] L. P. Gor'kov, J. Phys.: Condens. Matter **27**, 252001 (2015).

[30] H. Mirhosseini, M. Flieger, and J. Henk, New J. Phys. **15**, 033019 (2013).

[31] P. E. Blöchl, Phys. Rev. B **50**, 17953 (1994).

[32] M. Shishkin, M. Marsman, and G. Kresse, Phys. Rev. Lett. **99**, 246403 (2007).

[33] F. Fuchs, J. Furthmüller, F. Bechstedt, M. Shishkin, and G. Kresse, Phys. Rev. B **76**, 115109 (2007).

[34] M. Shishkin and G. Kresse, Phys. Rev. B **75**, 235102 (2007).

[35] M. Shishkin and G. Kresse, Phys. Rev. B **74**, 035101 (2006).

[36] J. P. Perdew, K. Burke, and M. Ernzerhof, Phys. Rev. Lett. **77**, 3865 (1996).

[37] H. J. Monkhorst and J. D. Pack, Phys. Rev. B **13**, 5188 (1976).

[38] M. Breitschaft, V. Tinkl, N. Pavlenko, S. Paetel, C. Richter, J. R. Kirtley, Y. C. Liao, G. Hammerl, V. Eyert, T. Kopp, and J. Mannhart, Phys. Rev. B **81**, 153414 (2010).

[39] R. A. Evarestov, E. Blokhin, D. Gryaznov, E. A. Kotomin, and J. Maier, Phys. Rev. B **83**, 134108 (2011).

[40] A. C. Garcia-Castro, M. G. Vergniory, E. Bousquet, and A. H. Romero, Phys. Rev. B **93**, 045405 (2016).

[41] C. Lasota, C.-Z. Wang, R. Yu, and H. Krakauer, Ferroelectrics **194**, 109 (1997).

[42] N. Sai and D. Vanderbilt, Phys. Rev. B **62**, 13942 (2000).

[43] R. Wahl, D. Vogtenhuber, and G. Kresse, Phys. Rev. B **78**, 104116 (2008).